PRELIMINARY DESIGN TOOL FOR POWER CONVERTERS IN ELECTRIC AIRCRAFT PROPULSION SYSTEMS

J. Kugener, A. Pal, S. Kazula
German Aerospace Center (DLR), Institute of Electrified Aero Engines, Department Component Technologies, Lieberoser Str. 13a, 03046 Cottbus, Germany

Abstract

In novel electric aircraft propulsion systems, the number and the power level of electrical and power electronic components increases significantly compared to conventional aircraft. Energy storage systems, such as batteries and fuel cells, provide direct current that needs to be regulated and conditioned. The speed and torque of the often proposed three-phase synchronous motors can be controlled by adjusting the frequency and the averaged amplitude of the terminal voltage. The conversion of electrical energy from one form to another is performed by power converters. Hence, optimized power converters are essential for power conversion, control and reliable operation of the electric drive train in electrified aero engines. In this paper, a preliminary design approach is presented to identify the different power converter components and their key characteristics for overall system studies. The volumetric and gravimetric power densities are derived from the preliminary design of their sub-components and compared to a prototype design of a 3-level Neutral Point Clamped (3L-NPC) inverter using commercially available components.

1. INTRODUCTION

The goals for limiting global warming to 1.5°C set at the Paris Agreement can only be achieved by significantly reducing greenhouse gas emissions. The aerospace industry is therefore exploring the application of all-, turbo- and hybrid-electric aircraft propulsion systems [1]. In this matter concepts for electric powertrains arise, which rely on power converters conditioning the electric power.

The functionality of switched power converters is enabled by sub-components such as diodes and transistors, which are based on the semiconductor technology. Here, rapid advancements in wide bandgap devices (WBG), i.e. Silicon Carbide (SiC) and Gallium Nitride (GaN), feature lower losses and the ability to operate at higher switching frequencies [2]. The amount of passive sub-components of converters such as capacitances and inductances decreases proportionally to the switching frequency. The resulting increased gravimetric and volumetric power densities call for advanced studies regarding the switching behaviour and hardware design to comply with the safety and reliability requirements in aviation. As a first step, preliminary design tools are useful to quickly estimate the characteristic properties and power densities for overall system studies.

A power converter is a highly optimized sub-component of the electric powertrain. During the preliminary design, there is often insufficient knowledge of the system, which is crucial for any optimization task. Numerous different components and complex correlations complicate an accurate estimation of weight, volume and losses. Furthermore, the limited scalability of semiconductor devices and the dominant influence of their packaging is often over-simplified in system studies [3–5], where only a rough value for a power converter power density is specified.

A more detailed estimation of the converters power density, including all respective sub-components, is a valuable contribution to system studies if a power converter topology is clearly specified, including all sub-components. In this paper, a general approach for such a preliminary sizing of power converters is introduced and applied. Analytical methods combined with empirical correlations based on commercially available sub-components are applied on an exemplary electric propulsion system. The design of SiC power modules and the associated scalability challenges are discussed. In order to provide an accurate indication of scalable power density, all sub-components are highlighted and examined. Assumptions on custom components such as busbars, which are dependent on structural design, will be matched to the dimensions of the selected semiconductors and validated with a digital Printed Circuit Board (PCB) prototype design.

As a reference case for the sizing approach, a preliminary design of a 3-level Neutral Point Clamped (3L-NPC) inverter is developed and implemented as a 3D model using commercially available components. The resulting design is checked for consistency with the gravimetric and volumetric outputs of the preliminary design tool. In addition, the resulting power densities are compared and discussed with

doi: 10.25967/610355

similar designs from the automotive industry and literature [6–10], emphazising the importance of the introduced approach.

2. ELECTRICAL POWER CONVERTERS AND THEIR COMPONENTS

A power converter is a complex system consisting of electronics as well as control, cooling and structural components. In order to ensure an accurate specification of power densities, a detailed indication and evaluation of all items considered is necessary. The specific components and their quantity strongly depend on the studied topology and the application [11].

2.1. Electric Propulsion Systems

This paper provides a brief overview of electrified aircraft propulsion topologies in FIG 1. All mentioned topologies and their subcategories are discussed in detail in literature [1, 2, 12]. It is important to note that a common attribute of all these topologies is the necessity for power converters conditioning electrical energy. The various types of power converters used in electric aircraft propulsion systems are discussed in subsection 2.3.

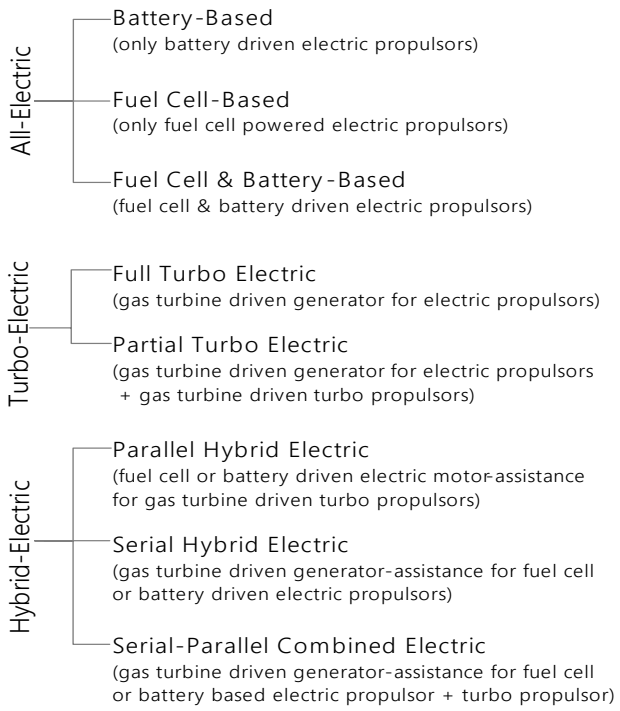

FIG 1. Topologies for electric aircraft propulsion [1]

A typical aircraft propulsion system can be divided into three subsystems consisting of an energy storage and power generation, a power train, and a propulsor. In a conventional aircraft propulsion system, a jet fuel is fed to a gas turbine engine, which drives a fan [2]. In an electrified aircraft, some of the subsystems could be replaced by electrical or electrochemical components. The potential electrified propulsion system topologies are divided into three categories according to the electrification of their components: all-electric, turbo-electric and hybrid-electric.

In an all-electric architecture, all components of the drive train are electrified. The energy source is an electrochemical energy unit, such as batteries or fuel cells. The power train consists of the power distribution system, power converters and electrical protection devices. The propulsion subsystem usually consists of an electric machine, a gearbox and a propulsor.

In a hybrid-electric powertrain the combination of a conventional and electrical topology is investigated. The energy source is divided into a fuel supplied subsystem and an electrochemical supplied subsystem. Analogous to the power supply, the thrust generation in this hybrid system can also be divided into an electric and a conventional subsystem. The different possibilities of hybridization in parallel, in series and in a parallel/series topology are discussed in more detail in [1].

In a turbo-electric aircraft, power is supplied by conventional or sustainable aviation fuel. Gas turbines drive electrical generators that feed an electrical grid. The propulsion unit consists of an electric motor to provide thrust. In a partial turbo-electric topology, an additional propulsor is connected to the gas turbine shaft and the generator is only driven with a share of the gas turbine power.

2.2. Aircraft Application Requirements

The feasibility of more electric aircraft correlates with high efficiency, high power density and high robustness of electrical components. An aircraft electrical system is an isolated grid providing and distributing power to all its electrified components [13]. Thus, a high reliability and high power quality are essential for the application. The service time of an aircraft under harsh environmental conditions is 100,000 hours [14]. A reliable operation of the converter and all its sub-components must be ensured over the entire service life to enable a save operation for the aircraft. The failure distribution among major power converter sub-components is shown in FIG 2.

The challenges of reduced ambient pressure, cosmic radiation, humidity and loss dissipation during the expected operation are discussed in various publications [14–19]. The focus point matrix from Wang and Blaabjerg [17] ranks the stressors vibration and mechanical shock on power electronic components as secondary to the main concerns of average temperature, temperature cycling and humidity for industry applications. The main sources of stress distribution for failures are illustrated in FIG 3. Reliability factors that result in a derating of the electrical components are presented in this paper and considered in the

preliminary design of the power converter. Further requirements, including mechanical and structural properties in accordance with the Environmental Conditions and Test Methods Standard for Airborne Equipment DO-160 [20], can significantly affect the resulting power density of a component. However, in a first design approach focusing on the electrical layout, these considerations are not addressed in detail.

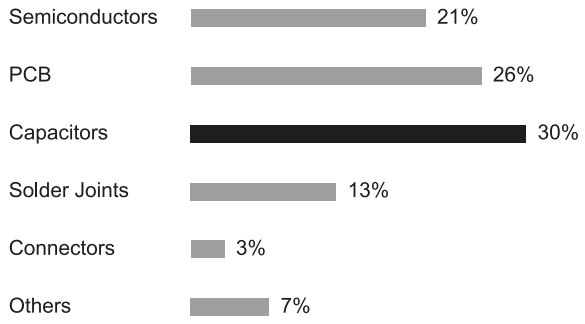

FIG 2. Failure distribution among major power converter components [19]

According to Paschen's law, at high altitudes the dielectric strength of the air decreases with the air pressure [15]. As a result, the thickness of the insulation layers or the clearance distance between electric items must be increased. According to the standard for insulation coordination for equipment in power supply systems EN60664, an altitude correction factor is applied depending on the maximum altitude. This factor more than doubles the safety distance at 8000 metres above sea level.

Furthermore, increased particle flux can lead to cosmic radiation induced failures as high-energy particles can induce single-event-burnout (SEB) failures in power semiconductors. To achieve low failure rates, it is recommended to operate silicon carbide (SiC) semiconductors at 70% and and silicon (Si) devices at 50% of the maximum breakdown voltage [18].

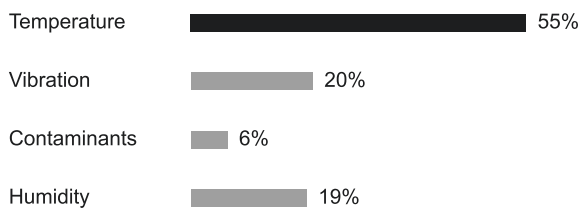

FIG 3. Source of stress distribution for failures [19]

To ensure high reliability, electrical components are operated below their rated power. Derating the components can extend their life, but this reduces the gravimetric and volumetric power density of the overall system. A complete system design must therefore consider a trade-off between different attributes to achieve an efficient overall system.

2.3. Power Converters

Power converters are essential in an electrical network with different voltage levels and forms. The power electronic components ensure a stable network, controllability, high reliability of the overall system and transformation from alternating current (AC) to direct current (DC) and vice versa. Depending on the system architecture, different types of power converters are required. Different types of converters and a examplary usage are illustrated in FIG 4.

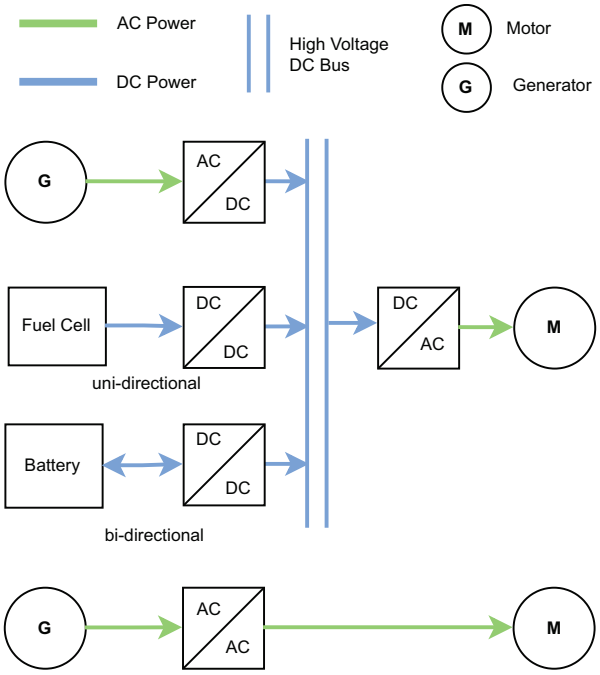

FIG 4. Overview of power converter types

2.3.1. AC-DC Power Converters

In active rectifiers, a three-phase alternating current is converted into a pulsed direct current. In hybrid and turbo-electric architectures, the electrical power of a generator is thus conditioned for the high voltage DC-bus. The aircraft active rectifier provides DC voltage regulation and power factor control on the generator side, while maintaining low total harmonic distortion in the generator currents [2].

2.3.2. DC-AC Power Converters

A three-phase inverter converts a direct current into a three-phase alternating current of any selected frequency in a specified range. An inverter enables the control of a potential electric motor in electric aircraft propulsion systems. Bidirectional inverters also enable regenerative braking. The most common inverter topology is the 2-level inverter B6-topology consisting of 3 half bridges i.e. 6 switches. At higher voltages, a multilevel topology can be advantageous to reduce the stress on the semiconductors and the machine winding, because the voltage stress is reduced by the amount

of levels. The 3-level neutral point clamped topology implemented in this work is further explained in subsection 2.9. Potentials and comparison of inverter topologies for future all-electric aircraft propulsion are examined by Ebersberger in [11].

2.3.3. AC-AC Power Converters

A typical AC-AC matrix converter consists of 2 stages. In the first stage, an AC to DC converter rectifies the voltage. This is followed by a DC to AC converter, which provides a three-phase alternating current to drive a motor or other AC loads. The AC-AC converter enables voltage regulation and frequency modulation of an AC power supply.

2.3.4. DC-DC Power Converters

In electrified aircraft propulsion systems, electrochemical units could provide the energy for the electric power train. A DC-DC converter provides a stable electrical network and controllability of the DC bus voltage. Ensuring power source protection is essential.Bidirectional power flow capability permits battery charging when power demand exceeds supply. Possible topologies for electric aircraft propulsion systems are discussed by Swaminathan in [21].

2.4. Power Semiconductors

Power semiconductors are key components of all power converters, as they enable the conditioning of the electric current transmission. The advancement of power semiconductors with the emergence of wide bandgap semiconductors (WBG) is seen as a key factor for efficient and high power dense electric aircraft propulsion systems [2]. Silicon carbide and gallium nitride (GaN) allow lower conduction and switching losses and higher thermal endurance than conventional silicon devices. Furthermore, the WBG semiconductors enable an increased frequency range.

High switching frequencies offer an advantages by enabling the downsizing of passive components like capacitors, inductors, and transformers as discussed in subsection 2.5. This reduction in component size and weight translates into a more compact and lightweight power converter, a requirement for aircraft applications. Among the state of the art wide bandgap devices, SiC semiconductors promise promising applications for energy conversion in the near future. GaN devices are not yet ready to replace SiC devices due to their limited current capability and lower breakdown voltage levels [15, 22]. In summary, SiC semiconductors are considered the optimal choice for power conversion applications in the near future, promising increased efficiency and performance for aircraft applications [15].

The limited current capacity of a single switch in state of the art SiC metal-oxide semiconductor field-effect transistors (MOSFET) is illustrated in FIG 5. In high power applications, it may be necessary to parallel multiple chips to achieve the required current capacity. It should be noted, that there is a limit to the number of MOSFETs that can be connected in parallel [23–25]. Parallel switching is a sensitive application where current balancing and increased stray inductance must be considered.

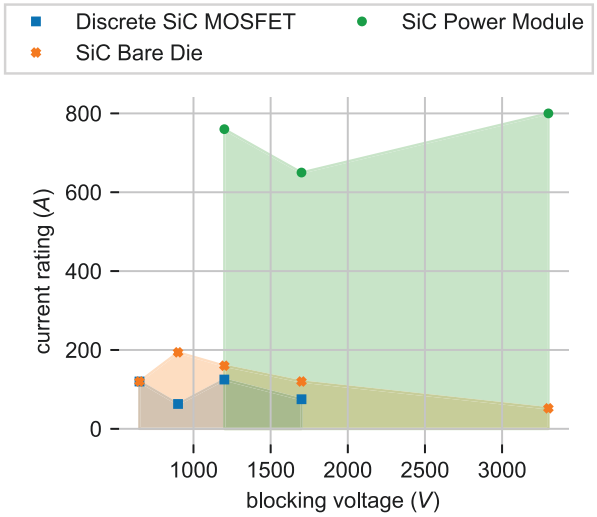

FIG 5. Maximum current capability for Wolfspeed SiC semiconductors [26]

The performance and dimensions of a semiconductor are significantly influenced by its packaging. Understanding the differences between a bare die, a discrete switch and a power module shown in FIG 6 is critical for power converter design [27].

A bare die is an unpackaged semiconductor chip. Although compact, a bare die requires additional packaging for integration into electronic systems and allows highly optimized module design for specific applications. The design of a power module for aircraft application requires specialized handling and expertise [28].

A discrete switch is a single semiconductor device in an individual package suitable for medium power applications. The packaged device can be incorporated directly into a hardware design.

A power module is a pre-packaged unit containing multiple power semiconductor devices. Designed for easy integration, power modules simplify the integration of power electronics, improve thermal management and handle higher power levels. They are commonly used in power converter designs.

In summary, bare dies, discrete devices and power modules differ in packaging, optimization focus and integration. Bare dies allow for highly optimized applications but require specialised handling. Discrete devices enable easy integration but are limited in current carrying capacity. Ease of integration and high current capability are combined in power modules.

However, commercial modules are rarely optimised for a specific application. The developed preliminary design tool incorperates electrical, dimensional and weight data of state of the art commercial power modules from various manufacturers.

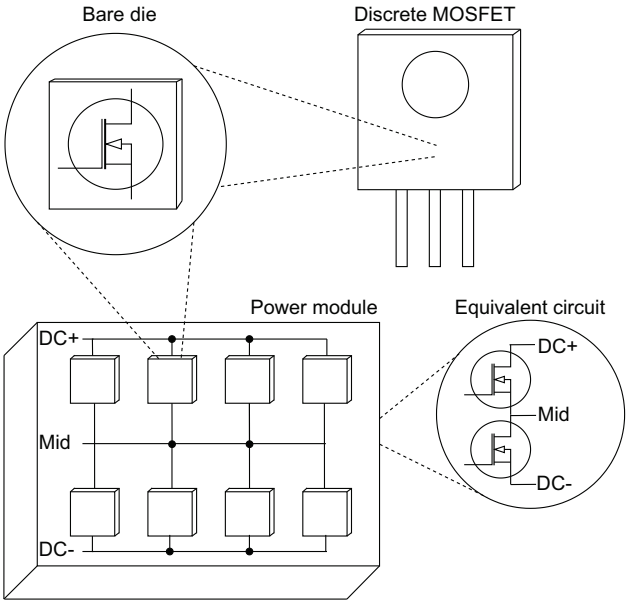

FIG 6. Comparison of SiC MOSFET packaging

2.5. DC-Link Capacitor

A DC link capacitor acts as an intermediate energy storage element to absorb energy during the transient switching process [29]. As the DC link capacitor provides a stable DC voltage, the selection of the appropriate capacitor type is crucial to ensure optimum performance, reliability and safety. This paper provides an overview of key DC link capacitor considerations. The design aspects include reliability and derating, losses, parallel connection of capacitors, weight and volume optimisation in the design of a capacitor bank [17, 29, 30].

Electrolytic capacitors are cost-effective and offer high capacitance values. However, they are more susceptible to degradation over time due to electrolyte drying, which limits their suitability for high reliability and long life applications. Ceramic capacitors offer compactness and high capacitance density. Their limited voltage ratings and susceptibility to piezoelectric effects make them more suitable for lower voltage applications [30]. Film capacitors, including metallized polypropylene film capacitors, offer stable capacitance and excellent self-healing properties [17]. Therefore, film capacitors are preferred for applications with high reliability requirement [30]. For the selection of the DC link capacitor, this paper focuses on metallized polypropylene film capacitors.

Component ageing and degradation can be caused by intrinsic and extrinsic factors such as design flaws, material wear out, operating temperature, humidity, mechanical stress, voltage and current. Wang [17] and Wechsel [30] divide into catastrophic events due to one-time overstress and wear out failures due to long-term degradation of capacitors. To increase the mean time between failures (MTBF), the voltage rating of the DC-link capacitor is commonly derated [17, 31]. The MTBF as a function of voltage derating based on the Military Handbook - Reliability Prediction of Electronic Equipment [32] is shown in FIG 7.

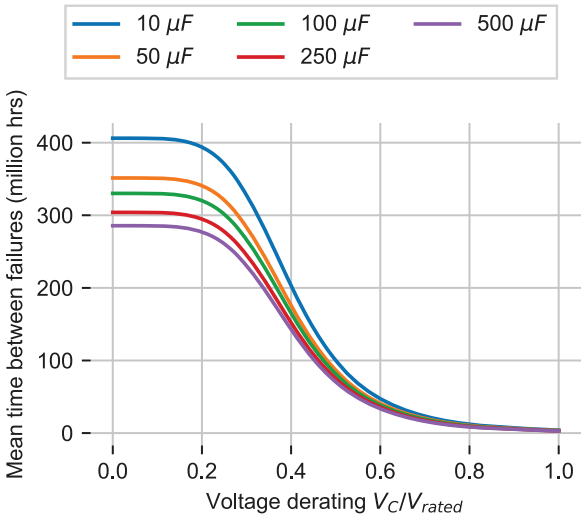

FIG 7. MTBF as a function of voltage derating [32] for different capacities

Paralleling capacitors increases the overall capacitance and the current handling capacity is increased due to current sharing of parallel components. Losses, i.e. heat, are distributed over a larger area. Accurate current sharing and voltage balancing are necessary for the optimization of the performance of paralleled capacitors, improving overall system reliability and extending capacitor life. Compact and lightweight DC link capacitors have a significant impact on overall system weight and volume. In the weight-sensitive aircraft propulsion system, the capacitor accounts for a significant proportion of the total converter weight [11]. The use of a compact capacitor bank, which accumulates multiple capacitors, ensures an optimised performance and increases the power density of the power converter.

2.6. Busbar

Busbars ensure the reliable flow of electrical current between different power electronic components, enabling efficient power distribution within the converter. With high current capacities and high switching frequencies, laminated busbars offer several advantages such as low impedance through tightly coupled conductive planes, simplified system assembly and improved reliability [33–35].

For the electrical design, the current amplitudes

and the various frequency components are responsible for the busbar thickness. The cross-sectional area of the busbar determines its current carrying capacity, e.g. $5A/mm^2$ [33]. Correct sizing is essential to prevent overheating and voltage drops.

The laminated busbar consists of conductive layers separated by thin insulating layers, as shown in FIG 8. $DC+$ and $DC-$ represent the positive and negative potential of the dc-link voltage bus. GND represents the grounding potential of the circuit. The layout of the busbar is determined by the dimensions of the power modules and the DC link capacitors, as well as their placement. Without considering the skin effect, the required current density decreases with the thickness of the busbar. However, increasing the thickness increases the weight of the propulsion system. It is therefore necessary to trade off the current density against the weight of the busbar based on the specific application.

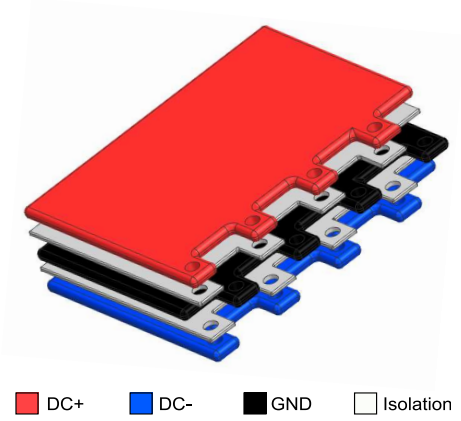

FIG 8. Structure of a laminated busbar [33]

2.7. Thermal Management

Efficient thermal management plays an important role in both the design and the operation of power converters in electric aircraft propulsion systems. With increasing power demands and limited space, efficiently dissipating the heat produced by power electronics components is essential to achieve high efficiencies and reliability. The power conversion losses have an even greater impact in compact designs [36]. Uneven heat dissipation or excessive temperatures can lead to reduced component efficiency, shortened life and potential critical failures. In aircraft applications, the decrease in air density at higher altitudes limits the effectiveness of conventional air fan cooling concepts. As a result, conventional air cooling proves insufficient to effectively remove heat and liquid cooling solutions have become widely accepted in inverter systems [6].

2.8. Enclosure and Structural Design

The enclosure acts as a protective barrier, shielding the power converter from environmental factors. The Environmental Conditions and Test Methods Standard for Airborne Equipment [20] defines requirements for key factors such as temperature, humidity, shock, vibration, liquid ingress, sand and dust, fungus resistance, radio frequency susceptibility, high intensity radiated fields, icing and fire. Test procedures are provided in [20] and [37] to ensure the long-term functionality of the power converter.

The selection of appropriate materials for the housing is critical. The choice of materials affects factors such as weight, durability and thermal conductivity. Consideration of the International Protection (IP) rating ensures the ability of the enclosure to protect against the ingress of solids and liquids and provides the required level of environmental protection [38].

Weight is a critical consideration in aircraft design. The materials and design of the enclosure should strike a balance between robustness and weight optimization. Granger [39] and Jones [40] suggest the use of a high proportion of carbon fibre, e.g. carbon fiber reinforced polymer (CFRP), in the structural design is suggested to meet the high gravimetric power density requirements. Hermetic sealing could allow electrical components to operate without derating due to the lower dielectric strength of air at high altitudes.

Power converters generate electromagnetic interference (EMI) due to high-frequency switching. As wide-band converter achieve higher switching frequencies [41], the excitation frequencies cover a much wider spectrum than conventional converters. The enclosure must provide effective shielding to keep EMI within acceptable limits. Interference with other avionics systems must be prevented and electromagnetic compatibility throughout the aircraft must be ensured in accordance with CS-25 [37].

2.9. The 3L-NPC Converter as Reference Case

Comparisions of various inverter topologies have been conducted in literature [11, 42, 43]. As a result, the 3-level Neutral-Point Clamped (3L-NPC) inverter topology stands as a promising choice for electric aircraft propulsion systems. The 3L-NPC inverter topology shown in FIG 9 is selected and investigated as a reference case.

The 3L-NPC inverter consists of three phase legs for the three-phase output current (U, V, W), shown in FIG 9. Each phase contains two half-bridge modules and one diode module illustrated in FIG 9. The midpoint of each half-bridge module is then connected to the neutral point over the clamped diode. The voltage stress over the switch is therefore reduced to half the DC-link voltage. The midpoint voltage, often referred to as the neutral point voltage, is stabilized by connecting the DC-link capacitors to the midpoint of each leg.

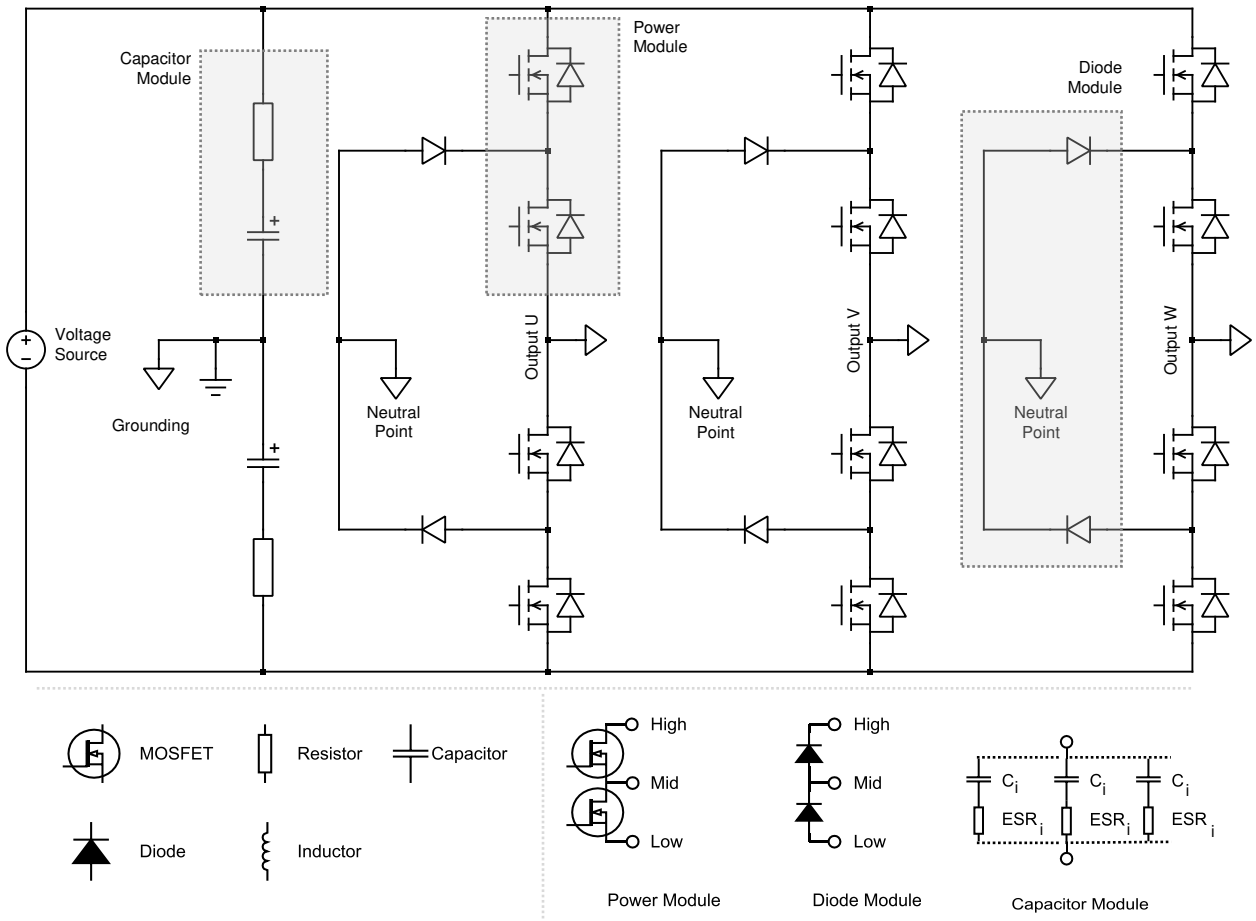

FIG 9. 3-level Neutral-Point Clamped (3L-NPC) inverter topology

The studied topology enables the generation of 3-level output voltages. The voltage stress on the power switches is significantly reduced and the overall efficiency is increased in comparison to a 2-level inverter. Moreover, the multiple voltage levels enable reduced switching losses and improved output waveform quality. Lower harmonic distortion allows for a smaller output filter design and lower stress on machine windings. Furthermore, the neutral-point clamping mechanism ensures balanced voltage sharing among the capacitors, reducing voltage fluctuations.

The 3L-NPC inverter topology aligns with the requirements of high power electric aircraft propulsion systems. Reduced losses and lower stresses on components contribute to efficient and reliable operation. Conversely, the probability of failure increases with the number of components and complexity of the control strategy. For this reason, it is important to have a good understanding of the inverter system and develop an optimised design. With a thoughtful design, the 3L-NPC topology is a strong candidate for inverters in an electric aircraft propulsion system.

3. SIZING APPROACH

A preliminary design for an inverter with a maximum output power rating P_N of 500 kW and a DC-link voltage V_{DC} of 1200 V is conducted. The sizing approach according to the implemented methods of the preliminary design tool for power converters in electric aircraft propulsion systems is applied.

3.1. Workflow

The main contributions of a preliminary sizing to a system study are power densities and efficiencies. An estimation of the mass, volume and power losses of a power converter is therefore performed. FIG 10 shows the principle workflow of the implemented preliminary design tool.

A topology is selected after obtaining various top-level requirements as input parameters. For a given topology, the preliminary electrical design is performed, including a first estimation of losses, voltage and current stress on the components. Based on the electrical design, the design of various sub-components such as power modules and capacitors is performed. The estimation of dimensions, volume and current density is the basis of the initial busbar design. Using a first approximation of volume and losses, the heatsink design is assumed.

Finally, the volume of each component and its mass are summed up to elaborate a volumetric and gravimetric power density. The losses of all components

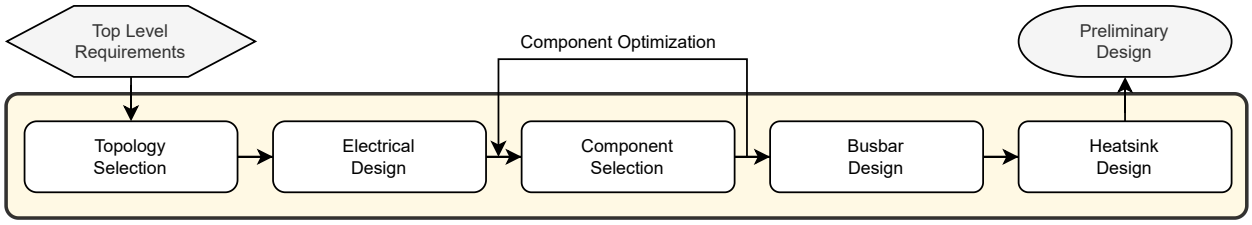

FIG 10. Workflow

are added together to calculate a first approximation of the converter efficiency. It is important to note that the preliminary results achieved by this approach do not replace accurate component design in a later phase of the development process. However, the results can assist an overall system assessment and an identification of correlations between different parameters.

3.2. Sizing of a 3L-NPC Inverter

From the input parameters, topology-specific calculations are performed to determine the initial attributes of the power converter. The output power P_N, the output phase voltage V_N and the output current I_N are calculated according to the equations 1 - 5 [44, 45].

$$P_N = 3 \cdot V_N \cdot I_N \cdot \cos\varphi \tag{1}$$

$$V_N = \frac{M_I}{\sqrt{2 \cdot 3}} \cdot V_{DC} \tag{2}$$

$$I_N = \frac{\sqrt{2} P_N}{M_I \cdot V_{DC} \cdot \cos\varphi} \tag{3}$$

The modulation index of an inverter M_I describes the ratio of the peak amplitude of the modulating signal to the peak amplitude of the carrier waveform used for pulse-width modulation control. The modulation index, ranging from 0 to 1, controls the inverter's output voltage V_N. At $M_I = 0$, the inverter is off. At $M_I = 1$, it reaches its peak voltage, usually the DC bus voltage in a voltage source inverter. For the reference case, the modulation index is fixed at 0.95.

$$M_I = \sqrt{2 \cdot 3} \cdot \frac{V_N}{V_{DC}} \tag{4}$$

The power factor $\cos\varphi$ measures the efficiency of power utilization in an electrical system. It quantifies the extent to which the electrical power S_N converts into active power P_N, such as mechanical motion or heat, as opposed to reactive power Q_N that creates magnetic or electric fields. A power factor of 1 signifies an ideal condition where all the supplied power is transformed into active power. For the reference case, the power factor is fixed at 0.95.

$$\cos\varphi = \frac{P_N}{S_N} \tag{5}$$

According to section 2, a voltage derating factor $df_{voltage}$ of the rated component voltage V_{rated} is applied to guarantee the safe operation of the inverter. The maximum voltage across the electronic components $V_{applied}$ is given by Equation 6. The applied voltage derating factor is fixed at 2.

$$df_{voltage} = \frac{V_{rated}}{V_{applied}} \tag{6}$$

The switching frequency has a significant influance on losses of the power converter and the dimensioning of passive elements. In the preliminary sizing tool, the value is given as an input parameter. For the reference design, the switching frequency is fixed at 20 kHz

The specific attributes included in the implemented tool are listed in Table 1.

TAB 1. Topology attributes

General input		
Output power	P_N	kW
DC-Link voltage	V_{DC}	V
Voltage ripple	ΔV_{DC}	%
Switching frequency	f_{SW}	kHz
Modulation index	M_I	
Power factor	$\cos\varphi$	
Topology specifications		
Output voltage	V_N	V
Output voltage level	$N_{V,level}$	
Output current	I_N	A
Module blocking voltage	V_{DS}	V
Number of power modules	N_{PM}	
Number of diode modules	N_{DM}	
Voltage derating factor	$df_{voltage}$	

3.3. Power Module

The power module design approach consists of two parts. First, the power losses are analytically calculated. Second, the dimensions of the implemented power modules are estimated. The following calculations according to the equations 7 - 12 [44–46] result in a preliminary loss assessment.

The voltage stress over the semiconductor switches is defined by the blocking voltage, i.e. the drain-source voltage V_{DS} in Equation 7. In the 3L-NPC converter topology, half of the DC link voltage is applied to the switches.

$$V_{DS} = \frac{1}{2} \cdot V_{DC} \tag{7}$$

The total power module losses $P_{PM,loss}$ are divided in switching losses $P_{PM,SW}$ and conduction losses $P_{PM,cond}$.

$$P_{PM,loss} = P_{PM,SW} + P_{PM,cond} \tag{8}$$

The switching losses P_{SW} are defined by the switching energy E_{SW} and increase with higher switching frequencies f_{SW}. The switching energy E_{SW} consists of the accumulated turn-on energy E_{on} and turn-off energy E_{off}.

$$E_{SW} = E_{on} + E_{off} \tag{9}$$

The resulting switching energy E_{SW} for state of the art power modules are illustrated in FIG 11 (a).

$$P_{PM,SW} = E_{SW} \cdot f_{SW} \tag{10}$$

The drain-source on-state resistance $R_{DS,on}$ characterizes the conduction losses $P_{PM,cond}$. The on-state resistance $R_{DS,on}$ for state of the art power modules are illustrated in FIG 11 (b).

$$P_{PM,cond} = R_{DS,on} \cdot I_{D,avg}^2 \tag{11}$$

The averaged drain current $I_{D,avg}$ is defined according to Equation 12.

$$I_{D,avg} = I_D \cdot \left(\frac{1}{8} + \frac{M_I \cdot \cos\varphi}{3\pi} \right) \tag{12}$$

For a more accurate result, gate driver, power loop, gate resistance R_G and temperature have to be considered. E_{on}, E_{off} and $R_{DS,on}$ are interpolated from the datasheet of various commercial power modules shown in FIG 11. The fitting parameters are then incorporated into the preliminary design tool.

FIG 12 does not reveal a distinct correlation between the current rating I_D and the module mass m_{pm} when examining commercially available half-bridge modules.

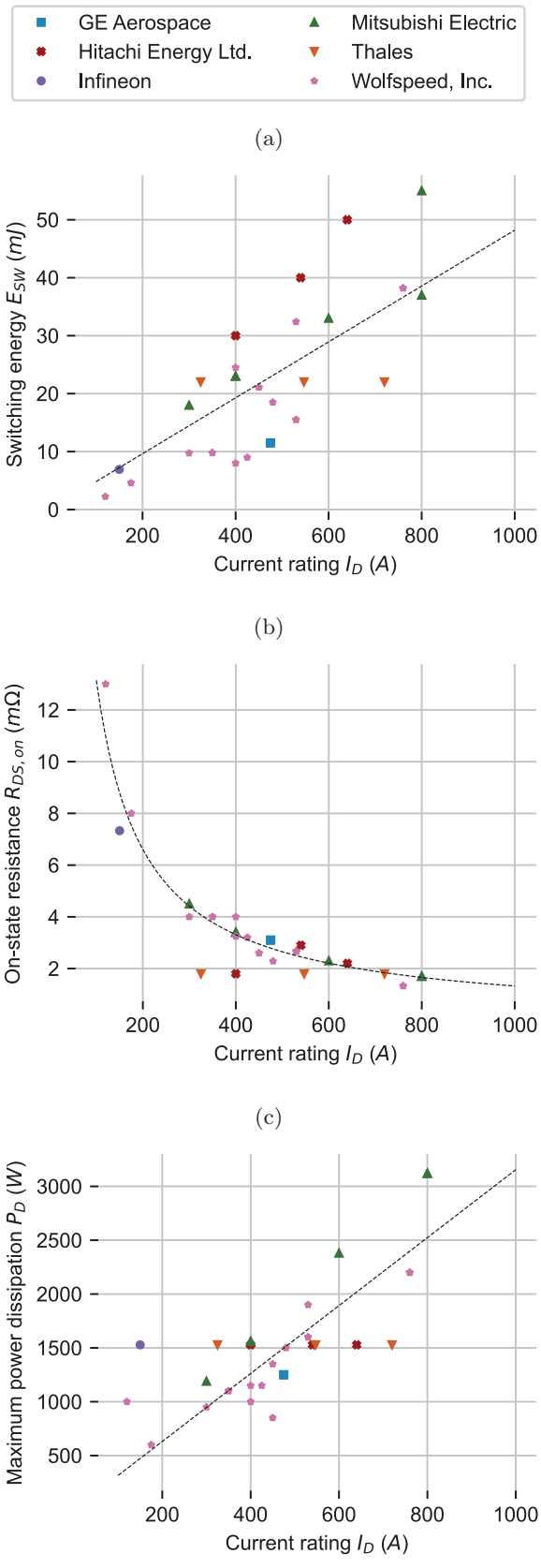

FIG 11. Electrical attributes of power modules
(a) switching energy (b) on-state resistance
(c) maximum power dissipation

Semiconductor manufacturers rarely specify the amount of parallel dies in the power module datasheet. In various publications [27, 47–49], images of thermal investigations and views into the packaging of commercially available modules reveal a typical amount of paralleled devices between 3 and 6. The approach of chip area optimization by Ebersberger [11] assumes a single die area between 10 mm^2 and 50 mm^2. An investigation of available Wolfspeed bare dies for a 1200 V blocking voltage shows a mean die area of 20 mm^2 [26]. The areas of the examined modules in FIG 12 (b) result in an average area of 66 cm^2, which results in a die coverage of less than 10 % of the total module area. This ratio demonstrates the low impact of the active semiconductor material on the overall weight of a power module.

A more significant factor is the packaging required for the safe operation of parallel chips. A more detailed analysis is required to estimate the accurate weight. At this preliminary stage, the weight of a power module is assumed to be constant. The airworthy power modules from Thales [50] are used as a reference for weight in this work. The mass of a half bridge module m_{PM} is therefore fixed at 200 g.

As for the volume V_{PM} of the considered power modules, FIG 12 (c) reveals a proportional relation between mass m_{PM} and volume V_{PM}. For the dimensions of the considered device from Thales, the area A_{PM} correlates to approximately 65 cm^2. The volume of a power module V_{PM} is fixed to 120 cm^3. The implemented power modules attributes are summerized in Table 2.

TAB 2. Power module attributes

Electrical specifications		
Maximum breakdown voltage	$V_{DS,max}$	V
Blocking voltage	V_{DS}	V
Drain-source current	I_{DS}	A
Turn-on energy	E_{on}	J
Turn-off energy	E_{off}	J
Drain-source on-state resistance	$R_{DS,on}$	$m\Omega$
Power loss		
Switching Losses	$P_{PM,SW}$	W
Conduction Losses	$P_{PM,cond}$	W
Total Losses	$P_{PM,loss}$	W
Module dimensions		
Mass	m_{PM}	g
Area	A_{PM}	mm^2
Volume	V_{PM}	mm^3

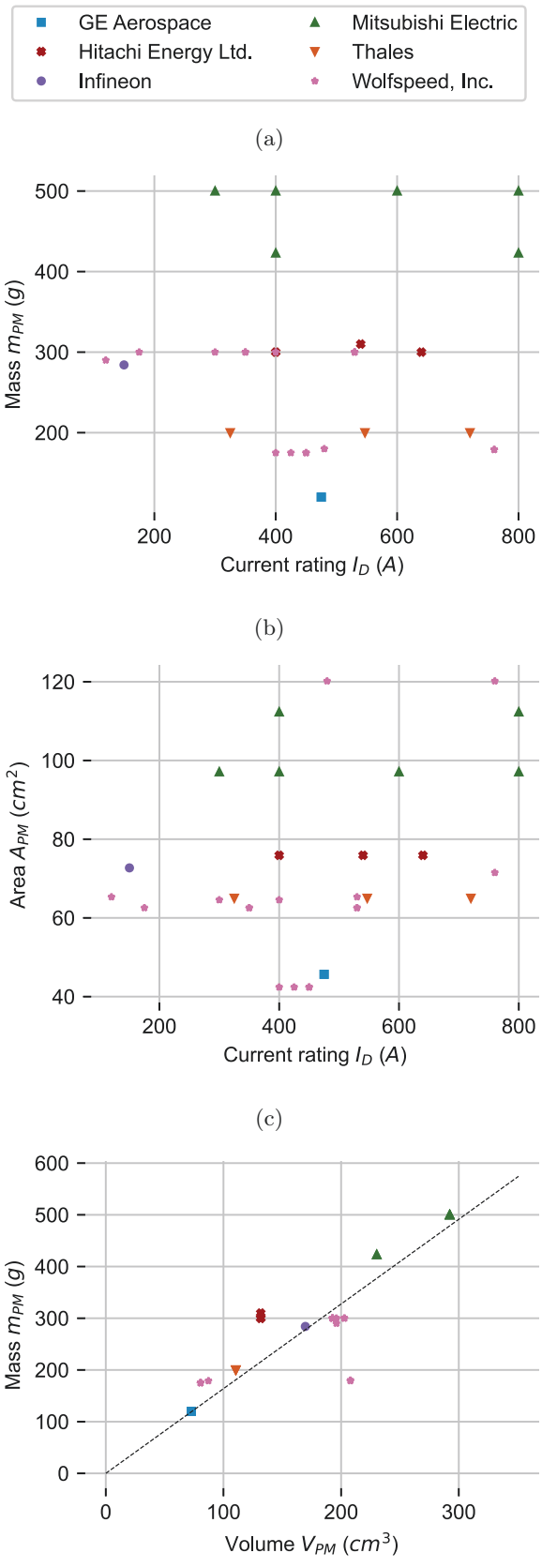

FIG 12. Power module mass and dimensioning
(a) mass (b) area (c) volume

3.4. Diode Module

Similar to the power module approach, the diode module design is divided into an electrical and a sizing part. The implemented design tool considers SiC Schottky diodes, due to their rapid switching capabilities and low voltage drop [11].

The neglectably low diode switching losses $P_{D,sw}$ are generally excluded from a loss assessment in a 3L-NPC converter [44]. The conduction losses $P_{D,cond}$ of a diode are defined by the forward voltage V_f and the forward current flowing through the diode I_f. For the loss assessment, the averaged forward current $I_{f,avg}$ is considered. The preliminary assessment of the power losses is implemented according to the equation 13 and 14 [44–46].

$$P_{DM,cond} = V_f \cdot I_{f,avg} \tag{13}$$

$$I_{f,avg} = I_f \cdot \left(\frac{1}{2\pi} - \frac{M_I \cdot \cos\varphi}{8} \right) \tag{14}$$

The forward voltage drop of a typical SiC Schottky diode as a function of current is shown in FIG 13. The interpolation parameters are incorporated in the preliminary design tool. The resulting conduction losses $P_{DM,cond}$ are shown FIG 14.

As with the power modules, the mass of the diode module m_{DM} is not determined by the active semiconductors but by the packaging. The investigated Wolfspeed diode modules CAR600M12HN6 [26] utilize the same packaging as for the MOSFET half bridges. The mass is therefore set at 200 g as well.

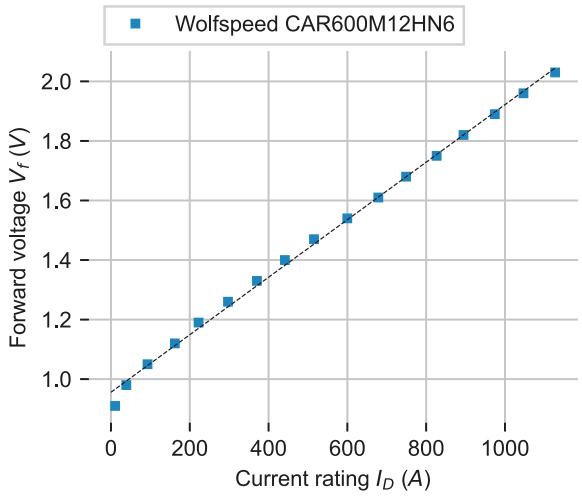

FIG 13. Diode forward voltage

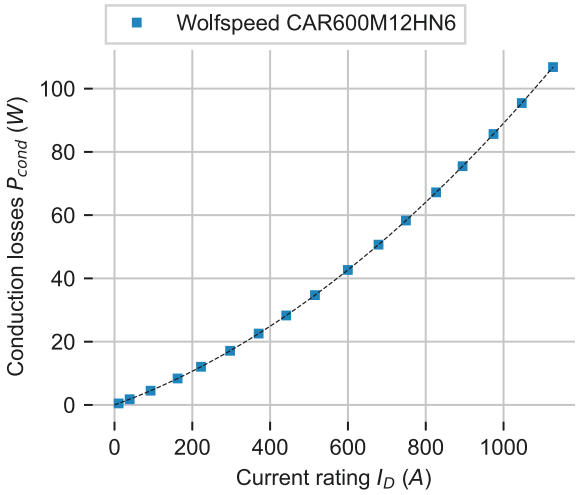

FIG 14. Diode conduction losses

The interpolated forward voltage as a function of the rated current is implemented in the preliminary design tool. All considered attributes are listed in Table 3.

TAB 3. Diode module attributes

Electrical specifications		
Maximum reverse voltage	$V_{R,max}$	V
Forward current	I_f	A
Diode Forward voltage	V_f	V
Power loss		
Conduction losses	$P_{DM,cond}$	W
Module dimensions		
Mass	m_{DM}	g
Area	A_{DM}	mm^2
Volume	V_{DM}	mm^3

3.5. DC-Link Capacitor

The capacitance C_C required to ensure a limited DC voltage fluctuation, called DC ripple ΔV_C, is given by Equation 15. The capacitance value varies with the switching frequency f_{SW}, modulation index M_I, current I_C, voltage V_C of the device and the output phase current I_N. The DC link capacitors are sized to stabilise the DC voltage and provide energy for fast current commutation [11]. The sensitivity of the overall capacitance to the switching frequency is illustrated in FIG 15.

$$C_C = \frac{\hat{I}_C}{2 \cdot \Delta V_C \cdot V_C \cdot f_{SW}} \tag{15}$$

$$I_C = I_N \sqrt{2M_I\left(\frac{\sqrt{3}}{4\pi} + \left(\frac{\sqrt{3}}{\pi} - \frac{9}{16}M_I\right)\cos^2\varphi\right)} \tag{16}$$

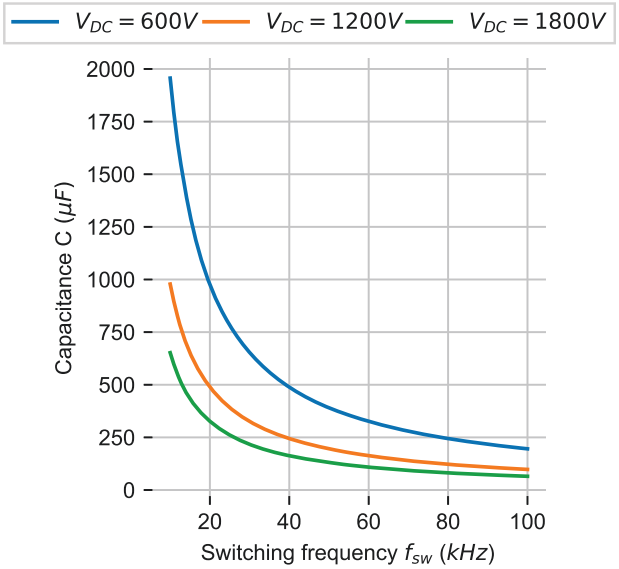

FIG 15. Capacitance C_C as a function of switching frequency f_{SW} for different voltage levels

Low stray inductance ESL_C and low equivalent series resistance ESR_C are essential to minimize losses [11]. As switching transients are not considered in this preliminary design, the inductance is neglected in the first design approach. However, it is important to note that leakage inductance is a key characteristic for the safe operation of power converters with WBG semiconductors [51]. The power loss $P_{C,loss}$ for a single capacitor C_i is given by Equation 17.

$$P_{C,loss} = ESR_C \cdot I_{C,i}^2 \tag{17}$$

FIG 16 shows the limitations in the current capability of a single capacitor. By parallelling a number of identical capacitors N_C, the total current I_C is divided by the number of paralled devices N_C.

$$I_C = N_C \cdot I_{C,i} \tag{18}$$

The total capacitance C_C is the sum of each capacitance $C_{C,i}$ connected in parallel. The total resistance ESR_C is less than the resistance of the smallest individual resistor $ESR_{C,i}$.

$$C_C = \sum_{i=1}^{N_C} C_{C,i} \tag{19}$$

$$\frac{1}{ESR_C} = \sum_{i=1}^{N_C} \frac{1}{ESR_{C,i}} \tag{20}$$

The behaviour described in the equations 18-20 is utilized to achieve higher current capabilities and lower power losses by paralleling multiple devices.

The goal of the design approach is to satisfy the equations 18 and 19 while achieving a low total mass. As seen in FIG 18 (a) and (b), mass and volume are proportional to the capacitance value. FIG 16 (a) shows a clear current limit, but no relation between current and capacitance or mass has been identified.

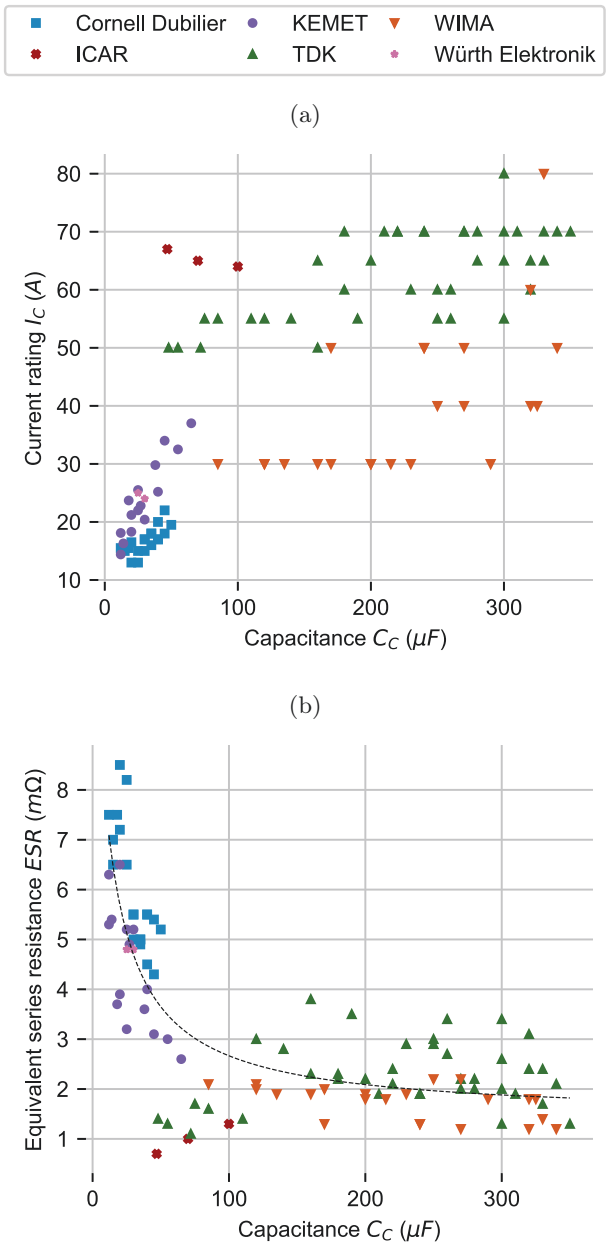

FIG 16. Capacitors Electrical attributes of (a) current rating (b) equivalent series resistance

To optimize the selection of capacitors, the constraints of the equations 18 and 19 are applied to the analyzed data set and the resulting capacitor configurations with the lowest total mass are selected for each operating point. To generalize the implemented approach, a multiple regression is applied to find a correlation between

the number of parallel components, capacitance value, current value and mass. The resulting Equation 21 is illustrated in FIG 17.

$$m_C = \alpha_0 + \alpha_1 \cdot C_C + \alpha_2 \cdot I_C + \alpha_3 \cdot (C_C \cdot I_C)^{\alpha_4} \quad (21)$$

With a coefficient of determination of 98.2%, the results of the regression show a high degree of agreement with the studied data set. With all the implemented parameters, summerized in Table 4, the approach enables a rapid evaluation of a DC link capacitor and provides an initial estimate of the dimensions, mass and losses according to the required capacitance and current rating.

TAB 4. DC-Link capacitor attributes

Electrical specifications		
Applied voltage	V_C	V
Total current	I_C	A
Total capacitance	C_C	μF
Number of parallel devices	N_C	
Power loss	$P_{C,loss}$	W
Specific Capacitor attributes		
Voltage rating	$V_{C,i}$	V
Current rating	$V_{C,i}$	V
Capacitance rating	$C_{C,i}$	A
Equivalent series resistance	$ESR_{C,i}$	$m\Omega$
Capacitor dimensions		
Mass	m_C	g
Area	A_C	mm^2
Volume	V_C	mm^3

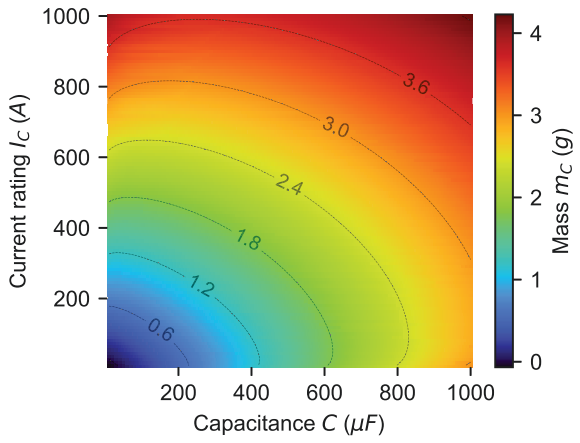

FIG 17. Capacitor current-capacitance-mass-relation

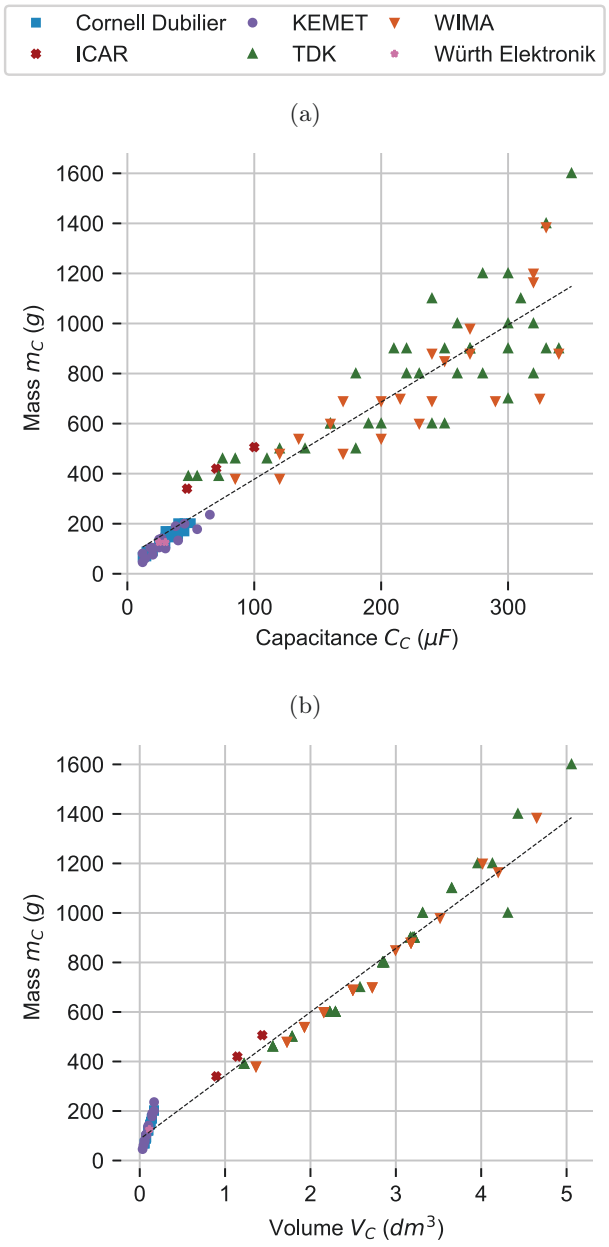

FIG 18. Capacitor mass and dimensioning
(a) mass (b) volume
(c) current-capacitance-mass-relation

3.6. Busbar

The design of the busbar is carried out with a simplified approach. The approach is based on an assumption of a busbar coverage A_{bus-s} of 75% of the connected components surface $A_{components}$. Each component is covered by two layers of a laminated busbar as shown in FIG 22. As the lamination is considered thin to the copper layer, the isolation density is neglected in an initial approach.

$$A_{bus-s} = 0.75 \cdot A_{components} \quad (22)$$

The components surface $A_{components}$ accumulates the number N_{PM} and area of power modules A_{PM}, the number N_{DM} and area of diode modules A_{DM} and the the number N_C and area of capacitors A_C.

$$A_{components} = N_{PM}A_{PM} + N_{DM}A_{DM} + N_C A_C \tag{23}$$

The cross-sectional area $A_{bus-c,layer}$ of one layer is determined from the current I_{bus} and an assumed current density J.

$$A_{bus-c,layer} = \frac{I_{bus}}{J} = h_{bus} \cdot w_{bus} \tag{24}$$

The maximum height of a busbar layer $h_{bus,layer}$ of 2 mm is fixed and the isolation thickness $h_{bus,iso}$ between the layers is assumed 1 mm. The total height of the busbar h_{bus} results by Equation 25.

$$h_{bus} = 2 \cdot h_{bus,layer} + h_{bus,iso} \tag{25}$$

The volume of the busbar results is defined by the with w_{bus}, the length l_{bus} and the height h_{bus} of the bus bar as defined in Equation 26. With a material density of copper ρ_{Cu} of 8.94 g/ cm^3, the total mass of the busbar m_{bus} can be estimated according to Equation 27.

$$V_{bus} = w_{bus} \cdot l_{bus} \cdot h_{bus} \tag{26}$$

$$m_{bus} = \rho_{Cu} \cdot V_{bus} \tag{27}$$

The results of a first estimation for the busbar mass are illustrated in FIG 19. The implemented attributes are summarized in Table 5.

TAB 5. Busbar attributes

Design specifications		
Current rating	I_A	A
Current density	J	A/mm^2
Material density	ρ	g/cm^3
Module dimensions		
Mass	m_{bus}	g
Surface area	A_{bus-s}	mm^2
Cross-sectional area	A_{bus-c}	mm^2
Volume	V_{bus}	mm^3

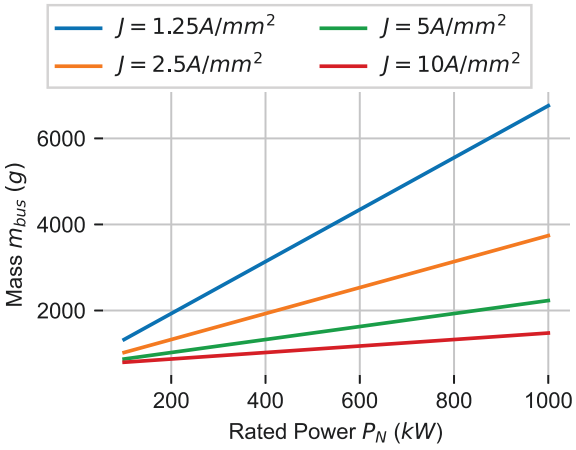

FIG 19. Busbar mass m_{bus} as a function of power rating P_N for various current densities J

3.7. Cold plate

The preliminary cold plate design is based on an commercial component used in the prototype design. The double-sided, aluminum friction stir welded cold plate accommodates up to six power modules.

As a reference cold plate, the Wieland MicroCool CP4009D [52] with a mass $m_{cp,ref}$ of 1500 g, designed for the Wolfspeed HM3 modules and optimized for the high heat flux of silicon carbide is considered. The reference cold plate allows a maximum power dissipation of 2200 W per module. To ensure save operation, the maximum power dissipation $P_{D,max}$ of the reference cold plate is downgraded by the factor of 2. A specific weight as a function of power rating is calculated according the maximum power dissipation in FIG 11.

$$m'_{cp} = \frac{2 \cdot m_{cp,ref}}{6 \cdot P_{D,max}} \tag{28}$$

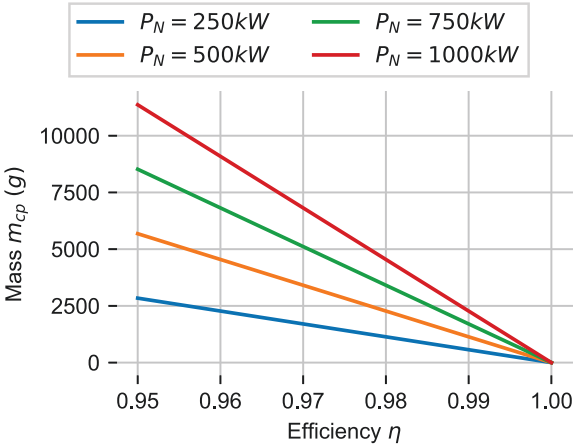

FIG 20. Cold plate mass m_{cp} as a function of converter efficiency η for various power ratings P_N

The specific mass is linearly scaled to the power losses of the power converter P_V. The resulting mass of the assumed cold plate is shown in FIG 20. The implemented attributes are summarized in Table 6. As part of the thermal system, the mass of the coolant depends on several factors of a peripheral system. It is therefore not included in the preliminary design.

TAB 6. Cold plate attributes

Reference specifications		
Reference mass	$m_{cp,ref}$	g
Reference height	h_{cp}	A/mm^2
Specific weight	m'_{cp}	g/W
Heatsink dimensions		
Mass	m_{cp}	g
Area	A_{cp}	mm^2
Volume	V_{cp}	mm^3

3.8. Enclosure

The total volume of the converter $V_{converter}$ in Equation 29 is composed of the sum of the component volumes $V_{components}$, the volume of the enclosure $V_{enclosure}$ and its thickness $t_{enclosure}$.

$$V_{converter} = V_{components} + V_{enclosure} = \left(\sqrt[3]{V_{components}} + 2 \cdot t_{enclosure}\right)^3 \tag{29}$$

The component volume defined in Equation 30 is increased by 20% to include unaccounted parts and larger clearances for safe operation at high altitudes.

$$V_{components} = 1.2 \cdot (N_{PM}V_{PM} + N_{DM}V_{DM} + N_C V_C + V_{bus} + V_{cp}) \tag{30}$$

As a high proportion of carbon fiber is suggested in subsection 2.8, the density of the enclosure will be defined by a proportion of carbon fiber reinforced polymer CFRP k_{CFRP} with a specific density ρ_{CFRP} and a reciprocal fraction of conventional aluminum k_{Al} with its specific density ρ_{Al} as defined in Equation 31.

$$\rho_{enclosure} = k_{CFRP} \cdot \rho_{CFRP} + k_{Al} \cdot \rho_{Al} \tag{31}$$

By varying the thickness of the enclosure $t_{enclosure}$ and the proportion of CFRP k_{CFRP}, a wide range of masses $m_{enclosure}$ illustrated in FIG 21 can be achieved as a first estimate for the casing.

$$m_{enclosure} = \rho_{enclosure} \cdot V_{enclosure} \tag{32}$$

The implemented attributes are summarized in Table 7.

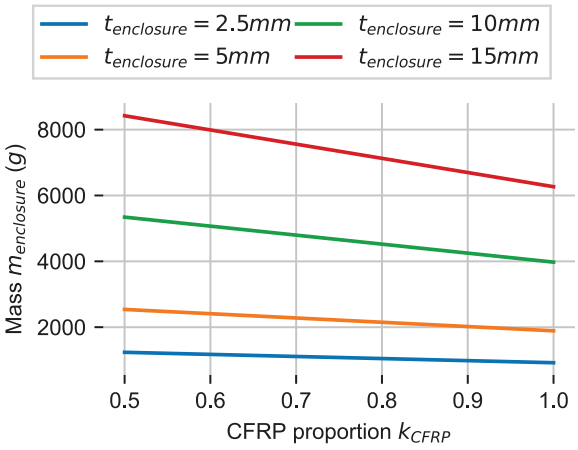

FIG 21. Enclosure mass $m_{enclosure}$ for different CFRP proportions k_{CFRP} and thickness $t_{enclosure}$

TAB 7. Enclosure attributes

Enclosure specifications		
Proportion of CFRP	k_{CFRP}	
Proportion of Al	k_{Al}	
Density of CFRP	ρ_{CFRP}	g/cm^3
Density of Al	ρ_{Al}	g/cm^3
Enclosure thickness	$t_{enclosure}$	mm
Enclosure dimensions		
Mass	$m_{enclosure}$	g
Components volume	$V_{components}$	mm^3
Enclosure Volume	$V_{enclosure}$	mm^3

3.9. Miscellaneous

In addition to the main factors contributing to the overall weight and volume of a power converter, the system is made up of several small lightweight components listed in Table 8. To account for these components, an additional mass m_{misc} of 1500 g is specified according to Nawawi [42].

TAB 8. Miscellaneous

Electrical components	Structural components
Gate drivers	PCB
Protection boards	Connectors
Power supply	Fixations
Sensors	Spacers
Microcontrollers	

TAB 9. Preliminary design results

Results	Units	Weight				Volume				Efficiency	
		component		total		component		total			
Power module	6	200	g	1200	g	122	cm^3	732	cm^3	98.70	%
Diode module	3	200	g	600	g	169	cm^3	366	cm^3	99.97	%
DC-Link Capacitor	2	1605	g	3210	g	1068	cm^3	2137	cm^3	99.97	%
Busbar	1	-		1476	g	-		164	cm^3	-	
Cold plate	1	-		1590	g	-		2632	cm^3	-	
Miscellaneous	1	-		1500	g	20	%	1206	cm^3	-	
Enclosure	1	-		2150	g	-		1181	cm^3	-	
Total				11726	g			8418	cm^3	98.64	%

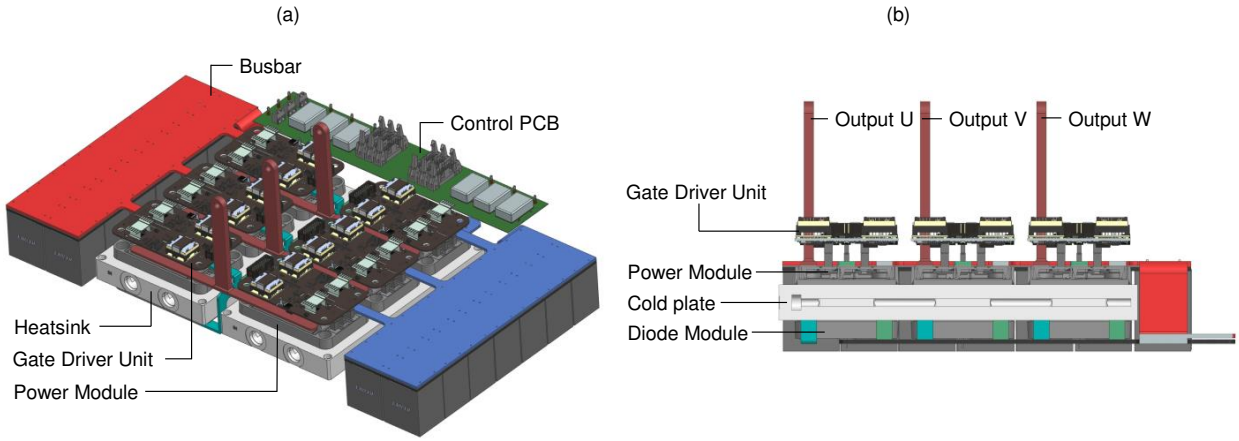

FIG 22. 3L-NPC prototype design
(a) isometric view (b) cross-sectional view

4. RESULTS

Table 9 shows the resulting data of a preliminary 3L-NPC inverter design with input data defined in Table 10. A gravimetric power density of 42 kW/ kg and a volumetric density of 59 kW/ L is achieved. The resulting power densites match state of the art converter designs from Fraunhofer IISB [7], NXP [8], Phi Power [9], Wolfspeed [10] and various automotive manufacturers summarized by Goli [6]. The comparison is illustrated in FIG 23.

The mass breakdown in FIG 25 shows that the total weight is not dominated by the semiconductor modules. Rather passive elements and cooling components account for more than half of the total weight. A comparative study for the weight distribution of the sub-components is conducted for a Wolfspeed 600 kW reference design CRD600DA12E-XM3 [10]. FIG 24 shows similar weight distribution for the specified sub-components. The proportion of 44% of undefined mass in the reference design is assumed an accumulation of the busbars, enclosure and structure.

TAB 10. Preliminary design input and assessment

Input data			
Output power	P_N	500	kW
DC-Link voltage	V_{DC}	1200	V
Voltage ripple	ΔV_{DC}	5	%
Switching frequency	f_{SW}	20	kHz
Modulation index	M_I	0.95	
Power factor	$\cos\varphi$	0.95	
Voltage derating factor	$df_{voltage}$	2	
Preliminary design assessment			
Efficiency	η	98.64	%
Mass	m	11.72	kg
Volume	V	8.41	L
Volumetric density	pd_v	59	kW/L
Gravimetric density	pd_g	42	kW/kg

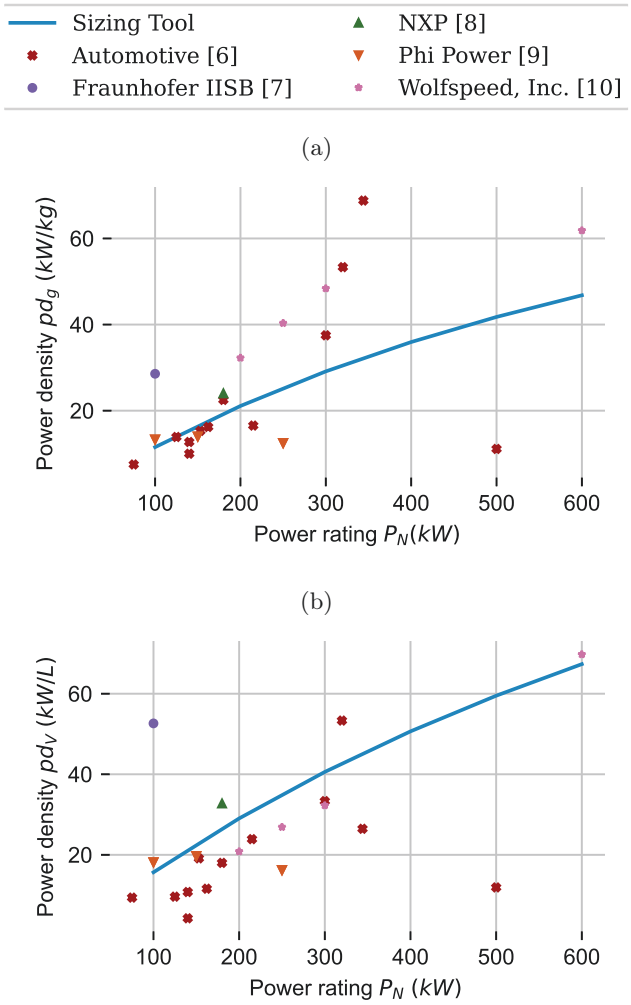

FIG 23. Comparision of power densities
(a) gravimetric (b) volumetric

The volumetric distribution in FIG 26 shows an essential proportion of the heat sink and the capacitor. The digital protoype design in FIG 22 has a volume of 6497 cm^3 without enclosure. With the assumed enclosure for the reference design of 1181 cm^3, the prototype achieves a volumetric power density of 65 kW/ L, which is in good agreement with the result of 59 kW/ L from the preliminary design tool.

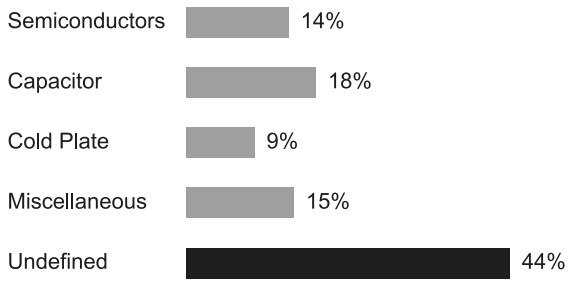

FIG 24. Mass breakdown of Wolfspeed reference design [10]

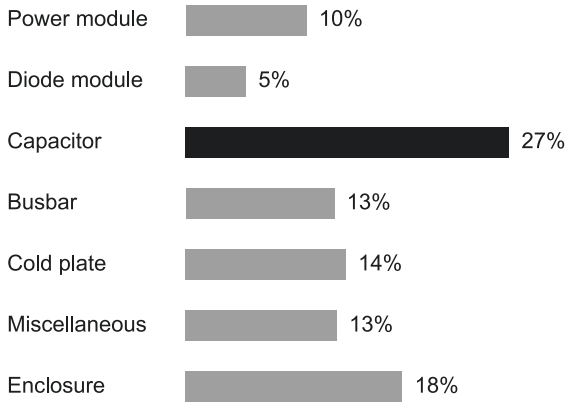

FIG 25. Mass breakdown of preliminary design

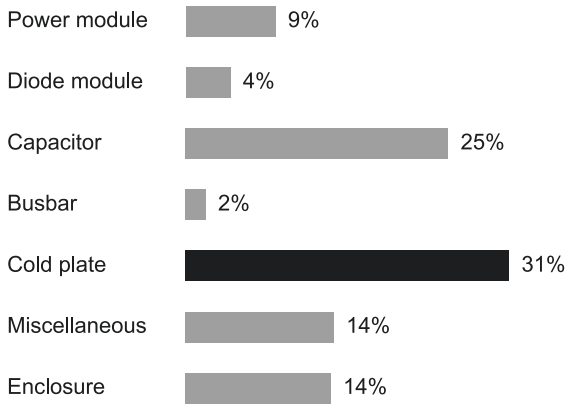

FIG 26. Volume breakdown of preliminary design

5. CONCLUSION

The preliminary results of an inverter design in section 4 highlight that the total weight and volume is not dominated by the semiconductor modules. Rather, passive elements and cooling components account for more than half of the total value.

The challenge of scaling semiconductors is discussed in subsection 2.3. The small proportion of active semiconductor area in the total power module area explains that the sensitive active materials have only a small impact on power density and rather the packaging required for reliable operation is a more significant factor. For a preliminary design, this paper assumes a constant weight and volume for the used power modules, while highlighting the limited scaling possibilities and operating areas of state of the art semiconductor materials.

Table 9 provides a first estimation of the system efficiency. It is important to notice, that a detailed loss assessment, including operating temperature, skin-effect, gate driver attributes and busbar losses,

has to be conducted for an even more accurate result.

The mass and volume breakdown in FIG 25 and 26 provide a clear specification of all the components included in the power density assessment. To provide comprehensive input for a following system study, these information, as well as information about the modelling of the sub-components are transmitted. As the neglected components like the cooling fluid or output filters are specified, the results could be extended for more detailed studies.

As all the considered components are clearly defined and evaluated, this approach enables a rapid yet comprehensive evaluation of the power converter. The resulting characteristics can then be incorporated into system studies to move closer to sustainable aviation.

ACKNOWLEDGEMENT

We would like to thank Dr. Matthias Lang, Victor Bahrs, Dimitrios Dimos and Andres Lopez Pulzovan for their fruitful insights, interesting discussions and contributions on the capacity regression and CAD design, which have contributed to improving the results presented in this paper.

NOMENCLATURE

Symbols

A	Area	$[mm^2]$
df	Derating factor	
E	Energy	[J]
ESL	Equivalent series inductance	$[nH]$
ESR	Equivalent series resistance	$[m\Omega]$
f	frequency	[Hz]
h	Height	$[mm]$
I	Current	[A]
J	Current density	$[A/mm^2]$
k	Proportion	
l	Length	$[mm]$
m	Mass	$[g]$
m'	Specific mass	$[g/W]$
M_I	Modulation index	
N	Amount	
P	Active power	[W]
pd_g	Gravimetric power density	$[kW/kg]$
pd_v	Volumetric power density	$[kW/L]$
Q	Electrical power	[VAR]
R	Resistance	$[\Omega]$
S	Reactive power	[VA]
t	Thickness	$[mm]$
V	Voltage	[V]
V	Volume	$[mm^3]$
w	Width	$[mm]$

Greek Symbols

α	Fitting parameter	$[^\circ]$
Δ	Difference/Fluctuation	
ρ	Material density	$[g/mm^3]$
φ	Phase angle	$[^\circ]$

Indices

$*_{-c}$	Cross-section
$*_{-s}$	Surface
$*_{AC}$	Alternating current
$*_{Al}$	Aluminium
$*_{avg}$	Average
$*_{bus}$	Busbar
$*_{CFRP}$	carbon fiber reinforced polymer
$*_{cond}$	Conduction
$*_{cp}$	Cold plate
$*_{Cu}$	Copper
$*_{C}$	Capacitor
$*_{DC}$	Direct current
$*_{DM}$	Diode module
$*_{DS}$	Drain-source
$*_{D}$	Drain
$*_{f}$	Forward
$*_{iso}$	Isolation
$*_{loss}$	Losses
$*_{max}$	Maximum
$*_{N}$	Rated Value
$*_{off}$	Turn-off
$*_{on}$	Turn-on
$*_{PM}$	Power module
$*_{ref}$	Reference
$*_{R}$	Revers
$*_{SW}$	Switching
$*_{V,level}$	Voltage level

REFERENCES

[1] C.K. Sain, S. Kazula, L. Enghardt. Electric propulsion for regional aircraft - critical components and challenges. Proceedings of DLRK, Dresden, 2022.

[2] Joseph Benzaquen, JiangBiao He, and Behrooz Mirafzal. Toward more electric powertrains in aircraft: Technical challenges and advancements, volume 5. 2021. DOI: 10.30941/CESTEMS.2021.00022.

[3] Stefan Biser, Guido Wortmann, Swen Ruppert, Mykhaylo Filipenko, Mathias Noe, and Martin Boll. Predesign considerations for the dc link voltage level of the centreline fuselage fan drive unit. Aerospace, 6(12):126, 2019. DOI: 10.3390/aerospace6120126.

[4] J.-K. Mueller, A. Bensmann, B. Bensmann, T. Fischer, T. Kadyk, G. Narjes, F. Kauth, B. Ponick, J. Seume, U. Krewer, R. Hanke-Rauschenbach, and A. Mertens. Design considerations for the electrical power supply of future civil aircraft with active high-lift systems. 2018. DOI: 10.3390/en11010179.

[5] Anton N. Varyukhin, Pavel S. Suntsov, Mikhail V. Gordin, Viktor S. Zakharchenko, and Daniil Ya. Rakhmankulov. 2019 international conference on electrotechnical complexes and systems (icoecs): Ufa state aviation technical university, ufa, russia, 22 -25 october 2019 : proceedings. Energies, (1):179, 2019. DOI: 10.1109/ICOECS46375.2019.

[6] Chandra Sekhar Goli, Somasundaram Essakiappan, Prasanth Sahu, Madhav Manjrekar, and Nakul Shah. Review of recent trends in design of traction inverters for electric vehicle applications. pages 1–6, 2019. DOI: 10.1109/PEDG51384.2021.9494164.

[7] Fraunhofer IISB. 100 kw sic-inverter for automotive application, 2023. https://www.iisb.fraunhofer.de/content/dam/iisb2014/en/Documents/Research-Areas/vehicle_electronics/2017-05-08_FraunhoferIISB_Produktblatt_100kW-SiC-Inverter_WWW.pdf.

[8] NXP. Ev-inverterhd, 2023. https://www.nxp.com/design/designs/ev-power-inverter-control-reference-platform-gen-1:RDPWRINVERTER.

[9] Phi Power. Pm100 - pm250, 2023. https://www.phi-power.com/de/wechselrichter/.

[10] Wolfspeed. 600 kw xm3 high performance dual three-phase inverter, 2023. https://www.wolfspeed.com/products/power/reference-designs/crd600da12e-xm3/.

[11] Janine Ebersberger, Maximilian Hagedorn, Malte Lorenz, and Axel Mertens. Potentials and comparison of inverter topologies for future all-electric aircraft propulsion. IEEE Journal of Emerging and Selected Topics in Power Electronics, 10(5):5264–5279, 2022. ISSN: 2168-6777. DOI: 10.1109/JESTPE.2022.3164804.

[12] Manuel A. Rendón, Carlos D. Sánchez R., Josselyn Gallo M., and Alexandre H. Anzai. Aircraft hybrid-electric propulsion: Development trends, challenges and opportunities. Journal of Control, Automation and Electrical Systems, 32(5):1244–1268, 2021. ISSN: 2195-3880. DOI: 10.1007/s40313-021-00740-x.

[13] Giampaolo Buticchi, Serhiy Bozhko, Marco Liserre, Patrick Wheeler, and Kamal Al-Haddad. On-board microgrids for the more electric aircraft—technology review. IEEE Transactions on Industrial Electronics, 66(7):5588–5599, 2019. ISSN: 0278-0046. DOI: 10.1109/TIE.2018.2881951.

[14] Hendrik Schefer, Leon Fauth, Tobias H. Kopp, Regine Mallwitz, Jens Friebe, and Michael Kurrat. Discussion on electric power supply systems for all electric aircraft. IEEE Access, 8:84188–84216, 2020. DOI: 10.1109/ACCESS.2020.2991804.

[15] Markus Meindl, Martin Maerz, Florian Hilpert, and Christian Bentheimer. Power electronics design for a 50 pax hybrid-electric regional aircraft. 2023. DOI: 10.2514/6.2023-4545.

[16] Daniel J. Lichtenwalner, Akin Akturk, James McGarrity, Jim Richmond, Thomas Barbieri, Brett Hull, David Grider, Scott Allen, and John W. Palmour. Reliability of sic power devices against cosmic ray neutron single-event burnout. Materials Science Forum, (924):559–562, 2018. DOI: 10.4028/www.scientific.net/MSF.924.559.

[17] Huai Wang, Marco Liserre, Frede Blaabjerg, Peter de Place Rimmen, John B. Jacobsen, Thorkild Kvisgaard, and Jorn Landkildehus. Transitioning to physics-of-failure as a reliability driver in power electronics. IEEE Journal of Emerging and Selected Topics in Power Electronics, 2(1):97–114, 2014. ISSN: 2168-6777. DOI: 10.1109/JESTPE.2013.2290282.

[18] Christian Felgemacher, Samuel Vasconcelos Araujo, Peter Zacharias, Karl Nesemann, and Artjom Gruber. Cosmic radiation ruggedness of si and sic power semiconductors. pages 51–54, 2016. DOI: 10.1109/ISPSD.2016.7520775.

[19] Huai Wang, Marco Liserre, and Frede Blaabjerg. Toward reliable power electronics: Challenges, design tools, and opportunities. IEEE Industrial Electronics Magazine, 7(2):17–26, 2013. ISSN: 1932-4529. DOI: 10.1109/MIE.2013.2252958.

[20] RTCA. Environmental conditions and test procedures for airborne equipment: Do-160, 2010.

[21] Niraja Swaminathan and Yue Cao. An overview of high-conversion high-voltage dc–dc converters for electrified aviation power distribution system. IEEE Transactions on Transportation Electrification, 6(4):1740–1754, 2020. DOI: 10.1109/TTE.2020.3009152.

[22] David Garrido-Diez and Igor Baraia. Review of wide bandgap materials and their impact in new power devices. pages 1–6, 2017. DOI: 10.1109/ECMSM.2017.7945876.

[23] Teresa Bertelshofer, Andreas Marz, and Mark.-M. Bakran. Limits of sic mosfets' parameter deviations for safe parallel operation. 2018.

[24] Shuhei Fukunaga, Alberto Castellazzi, and Tsuyoshi Funaki. Development of reliable multichip power modules with parallel planar- and trench-gate sic mosfets. pages 181–184, 2022. DOI: 10.1109/ISPSD49238.2022.9813624.

[25] Helong Li, Wei Zhou, Xiongfei Wang, Stig Munk-Nielsen, Daohui Li, Yangang Wang, and Xiaoping Dai. Influence of paralleling dies and paralleling half-bridges on transient current distribution in multichip power modules. IEEE Transactions on Power Electronics, 33(8):6483–6487, 2018. ISSN: 0885-8993. DOI: 10.1109/TPEL.2018.2797326.

[26] Wolfspeed. Silicon carbide power & gan rf solutions | wolfspeed, 2023. https://www.wolfspeed.com/.

[27] Haksun Lee, Vanessa Smet, and Rao Tummala. A review of sic power module packaging technologies: Challenges, advances, and emerging issues. IEEE Journal of Emerging and Selected Topics in Power Electronics, 8(1):239–255, 2020. ISSN: 2168-6777. DOI: 10.1109/JESTPE.2019.2951801.

[28] Y. Chen, A. Iradukunda, H. A. Mantooth, Z. Chen, and D. Huitink. A tutorial on high-density power module packaging. IEEE Journal of Emerging and Selected Topics in Power Electronics, 11(3):2469–2486, 2023. ISSN: 2168-6777. DOI: 10.1109/JESTPE.2022.3232691.

[29] N. I. Feng, WANG Qian, and L. I. Fei. Research on hybrid dc-link capacitor bank with high efficiency and long-life time. pages 611–615, 2019. DOI: 10.1109/EITCE47263.2019.9095086.

[30] Andrew Wechsler, Barrie C. Mecrow, David J. Atkinson, John W. Bennett, and Maamar Benarous. Condition monitoring of dc-link capacitors in aerospace drives. IEEE Transactions on Industry Applications, 48(6):1866–1874, 2012. ISSN: 0093-9994. DOI: 10.1109/TIA.2012.2222333.

[31] Haoran Wang, Huai Wang, Guorong Zhu, and Frede Blaabjerg. An overview of capacitive dc-links-topology derivation and scalability analysis. IEEE Transactions on Power Electronics, 35(2):1805–1829, 2020. ISSN: 0885-8993. DOI: 10.1109/TPEL.2019.2920257.

[32] U.S. Department of Defense. Military handbook - reliability prediction of electronic equipment: Mil-hdbk-217f, 1991.

[33] Zhongjing Wang, Yuheng Wu, Mohammad Hazzaz Mahmud, Zhao Yuan, Yue Zhao, and H. Alan Mantooth. Busbar design and optimization for voltage overshoot mitigation of a silicon carbide high-power three-phase t-type inverter. IEEE Transactions on Power Electronics, 36(1):204–214, 2021. ISSN: 0885-8993. DOI: 10.1109/TPEL.2020.2998465.

[34] Alan Dorneles Callegaro, Jing Guo, Michael Eull, Benjamin Danen, Jason Gibson, Matthias Preindl, Berker Bilgin, and Ali Emadi. Bus bar design for high-power inverters. IEEE Transactions on Power Electronics, 33(3):2354–2367, 2018. ISSN: 0885-8993. DOI: 10.1109/TPEL.2017.2691668.

[35] Zhao Yuan, Yalin Wang, Zhongjing Wang, Asif Imran Emon, Mustafeez ul Hassan, Fang Luo, and David Huitink. Insulation and switching performance optimization for partial-discharge-free laminated busbar in more-electric aircraft applications. IEEE Transactions on Power Electronics, 37(6):6831–6843, 2022. ISSN: 0885-8993. DOI: 10.1109/TPEL.2021.3137839.

[36] Che-Wei Chang, Xingchen Zhao, Ripun Phukan, Dong Dong, Rolando Burgos, and Arnaud PLAT. Weight-minimizing optimization of microchannel cold plate for sic-based power inverters in more-electric aircraft. pages 1–8, 2022. DOI: 10.1109/ECCE50734.2022.9947530.

[37] European Aviation Safety Agency. Certification specifications for large aeroplanes (cs-25), 2007.

[38] ISO. Iso 20653:2023: Road vehicles — degrees of protection (ip code) — protection of electrical equipment against foreign objects, water and access, 2023.

[39] Matthew Granger, David Avanesian, Ralph Jansen, Susanah Kowalewski, Alex Leary, Randy Bowman, Ariel Dimston, Erik Stalcup, and Wesley Miller. Design of a high power density, high efficiency, low thd 250kw converter for electric aircraft. 2021.

[40] Catherine E. Jones, Patrick J. Norman, Graeme M. Burt, Callum Hill, Giuliano Allegri, Jason M. Yon, Ian Hamerton, and Richard S. Trask. A route to sustainable aviation: A roadmap for the realization of aircraft components with electrical and structural multifunctionality. IEEE Transactions on Transportation Electrification, 7(4):3032–3049, 2021. DOI: 10.1109/TTE.2021.3078118.

[41] Li Zhang, Zhongshu Zheng, and Xiutao Lou. A review of wbg and si devices hybrid applications. Chinese Journal of Electrical Engineering, 7(2):1–20, 2021. ISSN: 2096-1529. DOI: 10.23919/CJEE.2021.000012.

[42] Arie Nawawi, Rejeki Simanjorang, Chandana Jayampathi Gajanayake, Amit K. Gupta, Chin Foong Tong, Shan Yin, Assel Sakanova, Yitao Liu, Yong Liu, Men Kai, Kye Yak See, and King-Jet Tseng. Design and demonstration of high power density inverter for aircraft applications. IEEE Transactions on Industry Applications, 53(2):1168–1176, 2017. ISSN: 0093-9994. DOI: 10.1109/TIA.2016.2623282.

[43] R. Yapa, A. J. Forsyth, and R. Todd. Analysis of sic technology in two-level and three-level converters for aerospace applications. 7th IET International Conference on Power Electronics, Machines and Drives (PEMD 2014), 2014. DOI: 10.1049/cp.2014.0498).

[44] Mohammed Hassan Ahmed, Mingyu Wang, Muhammad Arshad Shehzad Hassan, and Irfan Ullah. Power loss model and efficiency analysis of three-phase inverter based on sic mosfets for pv applications. IEEE Access, 7:75768–75781, 2019. DOI: 10.1109/ACCESS.2019.2922741.

[45] Raghbendra Tiwari and Roy Nilsen. Analytical loss equations for three level active neutral point clamped converters. Annual Conference of the IEEE Industrial Electronics Society, 2020. DOI: 10.1109/IECON43393.2020.9254393.

[46] Jonathan Dodge. 3l-anpc vs. 3l-npc inverters: Application note united sic. United SiC, 2021.

[47] Saeed Jahdi, Olayiwola Alatise, Jose Ortiz-Gonzalez, Peter Gammon, Li Ran, and Phil Mawby. Investigation of parasitic turn-on in silicon igbt and silicon carbide mosfet devices: A technology evaluation. 17th European Conference on Power Electronics and Applications, 2015. DOI: 10.1109/EPE.2015.7309093.

[48] Milad Maleki, Athanasios Mesemanolis, Lluís Santolaria, Antoni Ruiz, and Tobias Keller. High Power Density SiC Power Module for Formula E: Requirement, Design Considerations and the Test Results: International Exhibition and Conference for Power Electronics, Intelligent Motion, Renewable Energy and Energy Management : 3-7 May 2021. VDE, Frankfurt am Main, 2021.

[49] Julio Brandelero. Pwm power cycling of a multichip power module with active die temperature equalization. CIPS 2022; 12th International Conference on Integrated Power Electronics Systems, 2022.

[50] Thales. More electric flying with silicon carbide (sic) power modules, 2023. https://www.thalesgroup.com/en/markets/market-specific-solutions/microelectronics-solutions/microelectronics-addressed-markets-2.

[51] Jasper Schnack, Victor Golev, Jan Philipp Goerdes, Ulf Schuemann, Regine Mallwitz, and Stefan Stahl. Low-inductance dc-link design dedicated to sic-based highly integrated inverters. CIPS 2020; 11th International Conference on Integrated Power Electronics Systems, 2020.

[52] Wieland MicroCool. Cp 4009d - wieland microcool, 2023. https://www.microcooling.com/our-products/cold-plate-products/4000-series-standard-cold-plates/cp-4009d/.